[10$\bar{1}$0] Oriented Multichannel ZnO Nanowire Arrays with Enhanced Optoelectronic Device Performance

Dongqing He,[†,§] Xia Sheng,[†,§] Jie Yang,[†] Liping Chen,[†] Kai Zhu,*[‡] and Xinjian Feng*[†]

[†]Suzhou Institute of Nano-Tech and Nano-Bionics, Chinese Academy of Sciences, Ruoshui Rd. 398, Suzhou Industrial Park, Suzhou 215123, P. R. China

[‡]National Renewable Energy Laboratory, Golden, Colorado 80401, United States

S *Supporting Information*

ABSTRACT: Crystallographic orientation and microstructure of metal oxide nanomaterials have great impact on their properties and applications. Here, we report [10$\bar{1}$0] oriented ZnO nanowire (NW) arrays with a multichannel mesostructure. The NW has a preferential growth of low energy (10$\bar{1}$0) crystal plane and exhibits 2–3 orders of magnitude faster electron transport rate than that in nanoparticle (NP) films. Furthermore, the surface area of the as-prepared NW arrays is about 5 times larger than that of conventional NW arrays with similar thickness. These lead to the highest power conversion efficiency of ZnO NW array-based sensitized solar cells. We anticipate that the unique crystallographic orientation and mesostructure will endow ZnO NW arrays new properties and expand their application fields.

Manipulating the crystallographic orientation and microstructure of semiconductors are important to their properties and applications.[1−4] Aligned ZnO nanowire (NW) arrays have attracted considerable interest because of their tunable electronic properties and compatibility with a wide range of applications, such as UV lasing,[5] piezoelectric device,[6] photodetector,[7] solar cells,[8−10] and so on. Various synthesis methods including vapor-phase transport process,[11] chemical vapor deposition,[12] and liquid-phase approaches[13,14] have been developed for the fabrication of one-dimensional (1D) ZnO nanostructures. The key feature of 1D crystal growth follows the thermodynamic "lowest energy" rule where high energy crystal plane usually grows fast. As a result, ZnO NW arrays with a preferential growth of high-energy (0001) polar plane are commonly obtained. Consequently, both fundamental and application studies have been largely limited to [0001] oriented nanoarrays. Therefore, it is highly desirable to fabricate ZnO NW arrays with other preferential growth planes, such as low-energy {10$\bar{1}$0} nonpolar surfaces, and to investigate corresponding properties and applications.

Besides crystallographic orientation, microstructure of semiconductors is another important factor affecting their applications. Aligned 1D nanoarrays offer a directed charge transport path that makes them advantageous electrode architectures versus nanoparticles (NPs) for solar cell applications,[8−10,15,16] but the relatively low surface area caused from the free space between NWs has been a long-standing issue limiting their practical application. One strategy to increase the surface area is to increase the length of NWs, but efficiency up to 2.1% and 1.6% have been reported, respectively, for about 33 μm long ZnO NW and 60 μm long ZnO nanotube array-based dye sensitized cells (DSCs).[10,15] Herein, we report aligned [10$\bar{1}$0] oriented ZnO NW arrays with a multichannel mesostructure. The high surface area and rapid charge transport make the as-prepared NW arrays an ideal electrode structure for future optoelectronic device applications. We have demonstrated a solar to electricity conversion efficiency of 6.15%, to our knowledge, the highest value ever reported for 1D ZnO nanoarray-based DSCs. We believe that ZnO with such unique crystallographic orientation and mesostructure will be of broad academic and industrial interests.

Figure 1a is a typical field emission scanning electron microscopy (FE-SEM) cross-sectional view of densely packed
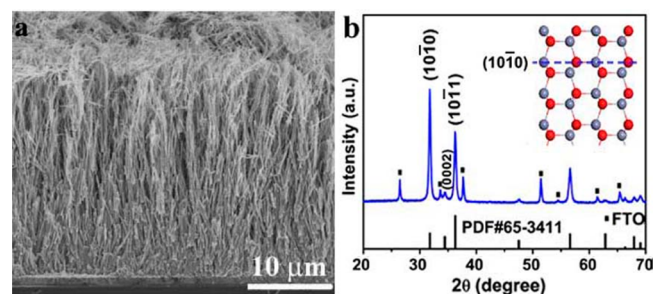
Figure 1. Aligned ZnO nanowire arrays. (a) FE-SEM cross-sectional view of ZnO NW arrays grown on FTO coated transparent glass substrate. (b) XRD pattern of the as-prepared NW arrays. Unlike conventional [0001] oriented NWs, the (10$\bar{1}$0) diffraction peak is much stronger than the others, and only a very weak (0002) peak was observed. The inset in panel b is an atomic structure model of wurtzite ZnO projected along [$\bar{1}$2$\bar{1}$0] with (10$\bar{1}$0) crystal plane being highlighted. Atom color code: red, O, and gray, Zn.

NW arrays that grow vertically from the fluoride doped tin oxide (FTO) coated transparent glass substrate. The NW arrays have a length of about 25 μm and an average diameter varies from about 300 nm at the bottom to about 20 nm at the tip part. Figure 1b shows the X-ray diffraction (XRD) pattern. All peaks can be indexed to wurtzite structured ZnO (JCPDS card No. 65-3411). In contrast to the XRD patterns of standard powder (the bottom of Figure 1b) and [0001] oriented ZnO NW arrays that are

reported up to date,[5-14] the (10$\bar{1}$0) diffraction peak is much stronger than the others and only a very week (0002) peak is observed, implying that the as-fabricated ZnO NW arrays may have a [10$\bar{1}$0] crystallographic orientation. The inset in Figure 1b is an atomic structure model of wurtzite ZnO projected along the [$\bar{1}$2$\bar{1}$0] direction with the (10$\bar{1}$0) crystal facet being highlighted.

According to the transmission electron microscopy (TEM) images of multiple and representative individual ZnO NWs shown in Figure S1 (Supporting Information SI) and Figure 2a at
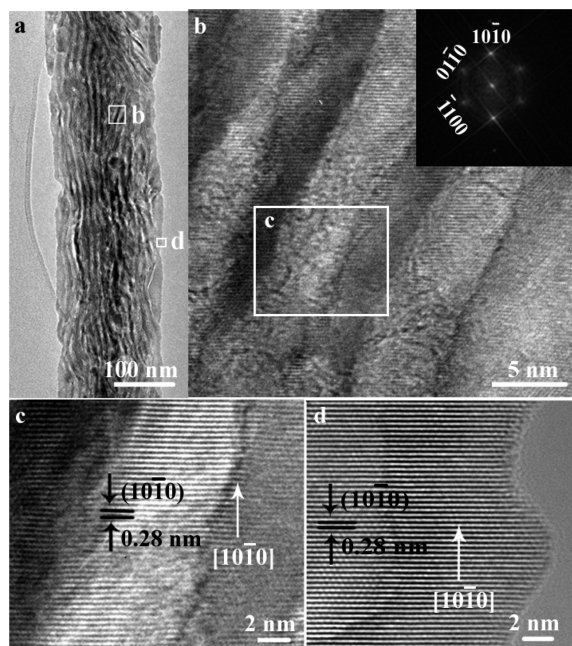

Figure 2. TEM and HR-TEM characterizations of ZnO nanowire. (a) Low magnification image of a single ZnO NW with multichannel mesostructure across the entire wire width. (b−d) HR-TEM images recorded from b, c, and d areas that marked by white small boxes in panels a and b, respectively, showing both nanochannel and crystalline framework, and confirmed that the growth is perpendicular to the (10$\bar{1}$0) crystal plane along the [10$\bar{1}$0] direction both at the center and border areas of NW. The inset in panel b is the corresponding FFT pattern.

different magnifications, the NW has internal nanochannels with an average width of about 6 nm and length that can be up to several micrometers. More detail information on the crystal structures of NW is gained from high-resolution TEM (HR-TEM) images. As shown in Figure 2b, the continuous crystal lattice across these nanochannels and the corresponding fast Fourier transform (FFT) patterns with minor distortions reveal a single-crystal-like feature of the ZnO NW. HR-TEM images of the center (Figure 2c) and edge (Figure 2d) areas of the NW as marked with white boxes in Figure 2b,a, respectively, show that the crystallographic orientation is the same at different areas. Clear fringe spacing of 0.28 nm corresponds to the d-spacing of the (10$\bar{1}$0) planes of ZnO can be observed. These XRD pattern and HR-TEM characterizations confirm that the as-synthesized ZnO NW arrays have a multichannel mesostructure and an unusual [10$\bar{1}$0] crystallographic orientation.

The as-obtained ZnO NW arrays were fabricated via a thermal phase transformation approach, during which materials with large crystal lattices can be readily converted to compacted ones by removing volatile products.[17-24] Herein, ZnO NW arrays are transferred from single crystal Zn(OH)F NW arrays, whose

morphology and crystal structures are shown in Figures S2 and S3, SI. Zn(OH)F NW arrays (JCPDS card #74-1816) grow vertically from the substrate along a preferential [001] direction. The length can be tuned to be longer than 40 μm by adjusting the growth time (Figure S4, SI). Figure 3 shows the schematics of the
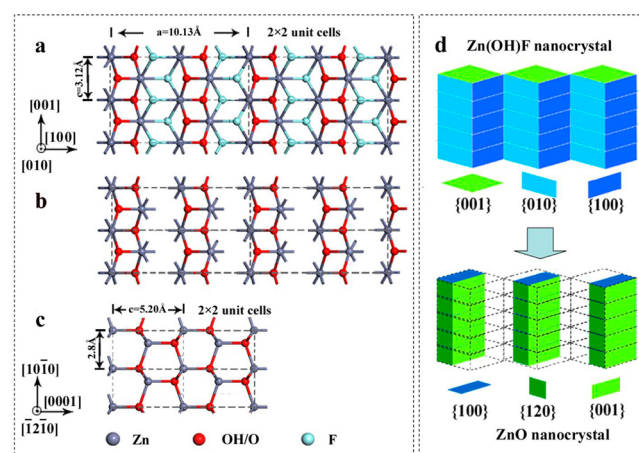

Figure 3. Schematics of structure transformation from Zn(OH)F to ZnO nanocrystals. (a) Atomic structure model of Zn(OH)F that is projected along [010] direction. (b) Structure model after F$^-$ and H$^+$ ions are removed. (c) Atomic structure model of ZnO projected along [$\bar{1}$2$\bar{1}$0] direction. (d) Illustration of the structure of solid Zn(OH)F (before) and multichannel ZnO nanocrystals (after transformation). Atom color code: cyan, F; red, O/OH; and gray, Zn.

transformation process. The crystal parameters for orthorhombic Zn(OH)F (Pna2$_1$) are a = 10.13 Å, b = 4.76 Å, and c = 3.12 Å. In this crystal, zinc atoms are located on the distorted octahedral sites.[25] Figure 3a shows a possible atomic structure model. Positions of zinc atoms in the (001) crystal plane of Zn(OH)F are separated by fluoride atoms and hydroxyl groups. During the thermal treating process, fluoride and hydrogen ions are removed from the lattice, leading to the formation of dangling bonds on zinc and oxygen atoms as shown in Figure 3b. Subsequently, oxygen and zinc atoms adjust their positions along a way with minimum lattice distortion to form more compacted ZnO nanocrystal (Figure 3c). Considering the large d-spacing of Zn(OH)F (100) planes (10.13 Å), which is similar to the 2-fold d-spacing of ZnO (0001) planes (5.2 Å), contraction of nanocrystal along the Zn(OH)F [100] direction is possible. An illustration of structural models of Zn(OH)F (before) and multichannel ZnO nanocrystals (after transformation) is shown in Figure 3d. The thermal treatment parameters, such as temperature and oxygen flow rate are critical to this contraction process. Under an appropriate condition, fluoride ion removal and crystal lattice contraction can be maintained at a dynamic equilibrium status, leading to the formation of single-crystal-like multichannel mesostructure.

Aligned ZnO NW arrays with such unusual crystal growth orientation and multichannel mesostructure will be of broad academic and industrial interests. In this work, we investigated their electronic properties and application as a photoanode in DSCs, where both rapid charge transport and high surface area are essential for high device performance.[1,2] As shown in Figure S5, SI, the surface area of the as-prepared multichannel NWs after being scratched off the substrate is measured to be 28.7 m^2/g. The roughness factor (RF) of our 25 μm long multichannel ZnO NW arrays is 955, which is comparable to that of most commonly

used NP films based photoanode (~1,000), but 5-fold larger than that of 1D ZnO NW arrays previously reported (RF < 200) with similar thickness.[9,10]

As we know, high surface area nanostructured electrode normally associated with NP films have large number of grain boundaries, lattice defects, and significantly low electron mobility.[26] To understand the electron transport in $[10\bar{1}0]$ crystal oriented ZnO NW arrays, they were analyzed using intensity-modulated photocurrent spectroscopy (IMPS).[27] Figure 4a compares the electron diffusion coefficient (D) as a
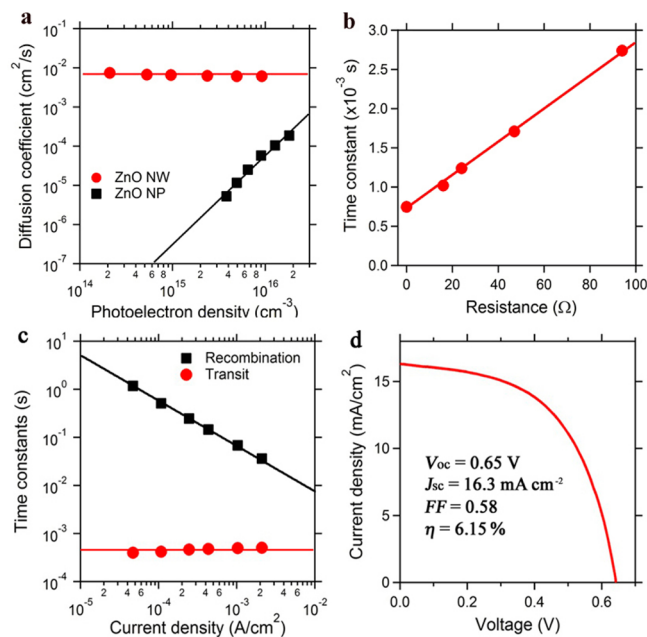
Figure 4. Electron transport, recombination, and current−voltage characteristics of ZnO NW array-based DSCs. (a) Dependence of electron diffusion coefficient on the photoelectron density based on ZnO NW arrays (red circle) and ZnO NP films (black square). (b) Transit time constants measured from IMPS as a function of serially connected external resistance (R_s). (c) Dependence of the electron transport and recombination times on photocurrent density determined by IMPS/IMVS at short circuit and open circuit, respectively. (d) The DSCs based on ZnO NW arrays give an open-circuit voltage of 0.65 V, a fill factor of 0.58, a short-circuit photocurrent density of 16.3 mA cm^{-2}, and a power conversion efficiency of 6.15%. The photocurrent was measured using AM-1.5 simulated sunlight (Oriel Sol3A Class AAA Solar Simulator).

function of photoelectron density. The D value of NP-based electrode displays the expected power-law dependence on the photoelectron density, which has been ascribed to electrons undergoing multiple trapping−detrapping events within an exponential distribution of conduction band tail states.[28] In marked contrast, the D value of ZnO NW is much higher and shows no dependence on the photoelectron density, indicating that either the surface trap distribution on ZnO NW arrays is very narrow in energy or the measured charge transport is limited by a factor unrelated to the transporting process within the ZnO NW arrays electrode.

In order to further understand such electron transport behavior, we connected ZnO NW array-based solar cells to external resistor with different resistances. Figure 4b shows the measured IMPS time constants (τ_c) of whole device as a function of the serially connected external resistance (R_s). The value of τ_c increases linearly with the resistance of the externally connected

resistors. The fitting to $\tau_c = (R_0 + R_s)C$ yields approximately $C = 2.2 \times 10^{-5}$ F and $R_0 = 32$ ohm. This result indicates that the τ_c from IMPS measurement is determined by the resistor− capacitor time constant of the devices,[26] rather than limited by the charge transport process within the ZnO NW arrays. Thus, the measured D value exhibits a photoelectron density independent behavior and represents only the lower bound for the actual diffusion coefficient of ZnO NW arrays, i.e., the true electron transport is much faster than that shown in Figure 4a. It is worth to note that, even with this underestimation, the apparent diffusion coefficients in $[10\bar{1}0]$ oriented ZnO NW arrays is 2 to 3 orders of magnitude higher than those in ZnO NP films, when compared over a broad range of photoelectron density. These results confirmed that the as-prepared single-crystal-like ZnO NW arrays have not only high surface area but also rapid charge transport properties that make it an ideal electrode structure for future optoelectronic device applications.

To capitalize on the advantage of high surface area and rapid charge transport properties, we fabricated DSCs using 25 μm long ZnO NW array-based photoanode developed in this study. Figure 4c shows the dependence of electron recombination time (τ_t) and transport time (τ_c) on photocurrent density of the cells. The τ_c value of ZnO NW array-based DSCs at short circuit does not change with increasing light intensity, which is consistent with the diffusion coefficient being independent of the photoelectron density (Figure 4a). In contrast, the τ_t value decreases (or recombination rate accelerates) with increasing light intensity, which can be attributable to the increased local concentration of injected electrons. The transport time is 2−3 orders of magnitude shorter than the recombination time across the entire illumination intensity range, indicating that the electron collection efficiency (η_{cc}) of our 25 μm long high surface area ZnO NW arrays is about 100%, as described by the relationship $\eta_{cc} = 1 - (\tau_c/\tau_t)$.[29]

As shown in Figure 4d, under simulated AM 1.5 illumination, DSCs based on ZnO NW arrays gives an open-circuit voltage (V_{oc}) of 0.65 V, a fill factor (FF) of 0.58, and a short-circuit photocurrent density (J_{sc}) of 16.3 mA cm^{-2} that is consistent with the incident photon-to-current efficiency measurement (Figure S6, SI). The power conversion efficiency is 6.15% without using a light scattering layer, which is the highest value ever reported for 1D ZnO NW array-based DSCs. Even when in comparison to the J_{sc} value (~17−18 mA/cm^2) of TiO$_2$ NP cells that were fabricated under highly optimized condition,[30,31] the J_{sc} value of our device is remarkable. As can be seen from Figure 1a, some NWs are entangled at the tip part that may hinder dye loading and ion movement in the electrolyte, which implies that the J_{sc} value and power conversion efficiency of our devices can be further improved if well-separated NW arrays can be achieved by using approaches such as supercritical drying techniques. The rapid charge transport and low recombination of our NW-based photoanode make it possible to use alternative redox shuttles with faster reduction kinetics but smaller overpotential than the traditional I$^-$/I^{3-} system to increase the V_{oc}.[32] Better device performance can be further obtained by employing more compatible dye or coating the electrodes with an ultrathin chemically more stable metal oxide layer, such as TiO$_2$, Nb$_2$O$_5$, or Al$_2$O$_3$.

In summary, we have constructed $[10\bar{1}0]$ oriented ZnO NW arrays with a multichannel mesostructure on transparent conductive substrate. The as-prepared ZnO NW arrays have both rapid electron transport and high surface area that make them ideal electrode materials for optoelectronic device

applications. We have demonstrated the highest power conversion efficiency of ZnO NW array-based sensitized solar cells. ZnO NW arrays with such unique crystal orientation and microstructure will be of broad academic and industrial interests, for example, for the use in piezoelectric devices, sensors, catalysis, light emission, solar cells, photodetectors, and so on.

■ ASSOCIATED CONTENT

Ⓢ Supporting Information

Experimental procedures, TEM image of multiple ZnO at low magnification, SEM, TEM, and XRD of Zn(OH)F NW arrays, dependence of the average length of Zn(OH)F NW arrays on the growth time, nitrogen adsorption−desorption isotherms, the corresponding pore size distribution within multichannel ZnO NW arrays, and the incident photon-to-current efficiency spectrum of DSSC based on multichannel ZnO NW arrays. This material is available free of charge via the Internet at http://pubs.acs.org.

■ AUTHOR INFORMATION

Corresponding Authors
*xjfeng2011@sinano.ac.cn
*kai.zhu@nrel.gov

Author Contributions
§These authors contributed equally to this work.

Notes
The authors declare no competing financial interest.

■ ACKNOWLEDGMENTS

■ REFERENCES

(1) Crossland, E. J. W.; Noel, N.; Sivaram, V.; Leijtens, T.; Webber, J. A. A.; Snaith, H. J. *Nature* **2013**, *495*, 215.

(2) Sheng, X.; He, D. Q.; Yang, J.; Zhu, K.; Feng, X. J. *Nano Lett.* **2014**, *14*, 1848.

(3) Feng, X. J.; Zhu, K.; Frank, A. J.; Grimes, C. A.; Mallouk, T. E. *Angew. Chem., Int. Ed.* **2012**, *51*, 2727.

(4) Liu, B.; Aydil, E. S. *J. Am. Chem. Soc.* **2009**, *131*, 3985.

(5) Huang, M. H.; Mao, S.; Feick, H.; Yan, H. Q.; Wu, Y. Y.; Kind, H.; Weber, E.; Russo, R.; Yang, P. D. *Science* **2001**, *292*, 1897.

(6) Wang, Z. L.; Song, J. H. *Science* **2006**, *321*, 242.

(7) Ji, L. W.; Peng, S. M.; Su, Y. K.; Young, S. J.; Wu, C. Z.; Cheng, W. B. *Appl. Phys. Lett.* **2009**, *94*, 203106.

(8) Baxter, J. B.; Aydil, E. S. *Appl. Phys. Lett.* **2005**, *86*, 053114.

(9) Law, M.; Greene, L. E.; Johnson, J. C.; Saykally, R.; Yang, P. D. *Nat. Mater.* **2005**, *4*, 455.

(10) Xu, C. K.; Shin, P.; Cao, L. L.; Gao, D. *J. Phys. Chem. C* **2010**, *114*, 125.

(11) Huang, M. H.; Wu, Y. Y.; Feick, H.; Tran, N.; Weber, E.; Yang, P. D. *Adv. Mater.* **2001**, *13*, 113.

(12) Wu, J. J.; Liu, S. C. *Adv. Mater.* **2002**, *14*, 215.

(13) Vayssieres, L. *Adv. Mater.* **2003**, *15*, 464.

(14) Greene, L. E.; Law, M.; Goldberger, J.; Kim, F.; Johnson, J. C.; Zhang, Y. F.; Saykally, R. J.; Yang, P. D. *Angew. Chem., Int. Ed.* **2003**, *42*, 3031.

(15) Martinson, A. B. F.; Elam, J. W.; Hupp, J. T.; Pellin, M. J. *Nano Lett.* **2007**, *7*, 2183.

(16) Varghese, O. K.; Paulose, M.; Grimes, C. A. *Nat. Nanotechnol.* **2009**, *4*, 592.

(17) Wang, X. D.; Gao, P. X.; Li, J.; Summers, C. J.; Wang, Z. L. *Adv. Mater.* **2002**, *14*, 1732.

(18) Zhou, L.; Smyth-Boyle, D.; O'Brien, P. *J. Am. Chem. Soc.* **2008**, *130*, 1309.

(19) Huang, Q. L.; Wang, M.; Zhong, H. X.; Chen, X. T.; Xue, Z. L.; You, X. Z. *Cryst. Growth Des.* **2008**, *8*, 1412.

(20) Feng, X.; Sun, L. T.; Dai, M.; Lu, Y. M. *J. Phys. Chem. C* **2010**, *114*, 15377.

(21) Li, L.; Yu, Y.; Meng, F.; Tan, Y.; Hamers, R. J.; Jin, S. *Nano Lett.* **2012**, *12*, 724.

(22) Wen, Z.; Zhu, L.; Li, L.; Sun, L.; Cai, H.; Ye, Z. *Dalton Trans.* **2013**, *42*, 15551.

(23) Xu, F.; Lu, Y.; Sun, L.; Zhi, L. *Chem. Commun.* **2010**, *46*, 3191.

(24) Gao, X.; Li, X.; Gao, W.; Qiu, J.; Gan, X.; Wang, C.; Leng, X. *CrystEngComm* **2011**, *13*, 4741.

(25) Serier, H.; Gaudon, M.; Demourgues, A.; Tressaud, A. *J. Solid State Chem.* **2007**, *180*, 3485.

(26) Zhu, K.; Kopidakis, N.; Neale, N. R.; Lagemaat, J. V. D.; Frank, A. J. *J. Phys. Chem. B* **2006**, *110*, 25174.

(27) Schlichthörl, G.; Huang, S. Y.; Sprague, J.; Frank, A. J. *J. Phys. Chem. B* **1997**, *101*, 8141.

(28) Cameron, P. J.; Peter, L. M. *J. Phys. Chem. B* **2005**, *109*, 7392.

(29) Schlichthörl, G.; Park, N. G.; Frank, A. J. *J. Phys. Chem. B* **1999**, *103*, 782.

(30) Nazeeruddin, M. K.; Filippo, D. A.; Fantacci, S.; Selloni, A.; Viscardi, G.; Liska, P.; Ito, S.; Takeru, B.; Grätzel, M. *J. Am. Chem. Soc.* **2005**, *127*, 16835.

(31) Yella, A.; Lee, H. W.; Tsao, H. N.; Yi, C.; Chandiran, A. K.; Nazeeruddin, M. K.; E. Diau, W. G.; Yeh, C. Y.; Zakeeruddin, S. M.; Grätzel, M. *Science* **2011**, *334*, 629.

(32) Hamann, T. W.; Jensen, R. A.; Martinson, A. B. F.; Ryswyk, H. V.; Hupp, J. T. *Energy Environ. Sci.* **2008**, *1*, 66.